Evidence for an impact-induced magnetic fabric in Allende, and exogenous alternatives to the core dynamo theory for Allende magnetization

Adrian R. Muxworthy[1],* Phillip A. Bland[2], Thomas M. Davison[1], James Moore[1], Gareth S. Collins[1], & Fred J. Ciesla[3]

[1]Department of Earth Science and Engineering, Imperial College London, London, UK.

[2]Department of Applied Geology, Curtin University of Technology, GPO Box U1987, Perth, Western Australia 6845, Australia.

[3]Department of Geophysical Science, University of Chicago, 5734 South Ellis Av., Chicago, IL 60430, USA

*Corresponding author:

Tel: +44 20 7594 6442

Email: adrian.muxworthy@imperial.ac.uk

Abstract

We conducted a paleomagnetic study of the matrix of Allende CV3 chondritic meteorite, isolating the matrix's primary remanent magnetization, measuring its magnetic fabric and estimating the ancient magnetic field intensity. A strong planar magnetic fabric was identified; the remanent magnetization of the matrix was aligned within this plane, suggesting a mechanism relating the magnetic fabric and remanence. The intensity of the matrix's remanent magnetization was found to be consistent and low (~6 μT). The primary magnetic mineral was found to be pyrrhotite. Given the thermal history of Allende, we conclude that the remanent magnetization formed during or

after an impact event. Recent mesoscale impact modeling, where chondrules and matrix are resolved, has shown that low-velocity collisions can generate significant matrix temperatures, as pore-space compaction attenuates shock energy and dramatically increases the amount of heating. Non-porous chondrules are unaffected, and act as heat-sinks, so matrix temperature excursions are brief. We extend this work to model Allende, and show that a 1km/s planar impact generates bulk porosity, matrix porosity, and fabric in our target that match the observed values. Bimodal mixtures of a highly porous matrix and nominally zero-porosity chondrules, make chondrites uniquely capable of recording transient or unstable fields. Targets that have uniform porosity, e.g., terrestrial impact craters, will not record transient or unstable fields. Rather than a core dynamo, it is therefore possible that the origin of the magnetic field in Allende was the impact itself, or a nebula field recorded during transient impact heating.

1. Introduction

Carbonaceous chondrite meteorites bear witness to the range of nebular and asteroidal processes that preceded large-scale planetary accretion. These meteorites contain two principal components: abundant sub-micron and micron-scale matrix materials that form a mineralogically complex aggregate; and mm-scale chondrules, the spherical igneous inclusions that give chondrites their name. The Allende meteorite is a member of the CV group of carbonaceous chondrites. Estimates of the age of the Solar System are based on analyses of components in Allende and other CV chondrites (Amelin et al., 2009). Allende is arguably the most analyzed rock on Earth, but, fundamental aspects of the record of early solar system processes, contained in this meteorite and others, remain poorly understood and a matter of vigorous debate. Their relatively pristine nature has driven the assumption that these meteorites derive from primitive asteroids. However, a body of work - paleomagnetic studies of Allende (Butler, 1972; Carporzen et al., 2011; Funaki and Wasilewski, 1999; Weiss et al., 2010), numerical modeling (Elkins-

Tanton et al., 2011; Sahijpal and Gupta, 2011) and compositional associations (Humayun and Weiss, 2011) - has prompted the recent suggestion that several chondrite groups are derived from a large differentiated parent asteroid: an object that had a convecting magma ocean, a liquid metallic core and an active dynamo field (Elkins-Tanton et al., 2011; Fu et al., 2014; Humayun and Weiss, 2011; Sahijpal and Gupta, 2011; Weiss et al., 2010).

Three processes are known to control the evolution of chondritic asteroids: (1) thermal metamorphism, (2) aqueous alteration and (3) impact-induced shock metamorphism. All three are significant in interpreting the paleomagnetic record in a meteorite. Shock metamorphism has not been considered a dominant process in the most primitive meteorites, the carbonaceous chondrites: 85% are ranked S1 ('unshocked'; <4-5GPa) or S2 ('very weakly shocked'; 5-10GPa) (Scott et al., 1992). The calibration here (assigning a shock level based on observed shock metamorphic textures, with an estimate of the required shock pressure to generate the textures, and the magnitude of post-shock heating) is based on impact recovery experiments on non-porous target rocks, or single crystals. Although both Stöffler et al. (1991) and Scott et al. (1992) noted the importance of porosity in determining shock level and impact heating, its significance has rarely been discussed in works applying the Stöffler et al. (1991) criteria to meteorites. This is unfortunate, as porous targets respond very differently to non-porous targets under shock. Porosity compaction attenuates shock energy in an impact and dramatically increases the amount of heating, as energy is expended crushing out the pore space (e.g., Ahrens and Cole, 1974; Kieffer, 1971; Melosh, 1989; Sharp and de Carli, 2006; Zel'Dovich and Raizer, 1967). The role of porosity is significant when we consider the impact record in carbonaceous chondrite meteorites, as the consensus view is that primordial carbonaceous parent bodies had significant micro-porosity. And it is particularly important when we consider the paleomagnetic record in meteorites. The interpretation of the paleomagnetism data that underpins the idea that primitive meteorites may come from differentiated asteroids is based on a number of assumptions. A fundamental one – drawing on Stöffler et al. (1991) – is that shock heating was minimal.

Allende is classified as shock stage S1 (Scott et al., 1992). Shock effects in the Stöffler et al. (1991) criteria are estimated based on metamorphic textures in large (>50-100μm) chondrule olivines. Shock effects in sub-μm matrix grains are rarely considered. Yet matrix is the host for the magnetic carrier phase. Watt et al. (2006) and Bland et al. (2011) found that the matrix in Allende has a micron-scale fabric. Bland et al. (2011) used fabric analysis to show that the volume of the primary matrix aggregate had been halved in an impact-induced compaction event (determining that the primary matrix porosity, pre-compaction, was of-order 70-80%). In addition to the fabric analysis of meteorite matrix, studies of experimentally synthesized fine-grained material (Blum, 2004; Blum and Schrapler, 2004), and modeled accreted aggregates (Ormel et al., 2008) indicates that primordial matrix porosities were in the 70-80% range. A review of chondrite porosity data (Macke et al., 2011; Sasso et al., 2009) by Bland et al. (Bland et al., 2014) supports this estimate. Static compression experiments indicate that gravitational compression was not significant in asteroids with radii <100 km (Blum, 2004). Impact-induced compaction is more efficient, and generates porosities similar to those seen in chondrites (Beitz et al., 2013). Taken together, and given the textural evidence for impact-induced compaction of initially highly porous matrix aggregates (Watt et al. 2006; Bland et al. 2011), the expectation is that primordial asteroids initially had high porosity, and that the dominant porosity-reduction process was impact-induced compaction. What was the effect of that compaction event on Allende matrix? What pressure and temperature did it experience? These questions have implications for our understanding of the paleomagnetic record in Allende and other (compacted) chondritic meteorites.

Although the dichotomy between porous and non-porous targets was well known in the impact community, until recently there had been no numerical studies of shock in materials with a bimodal distribution of porous and non-porous components, i.e., a material approximating a chondritic meteorite: (nominally) zero-porosity spherical chondrules (0.1-1mm in size) set in a highly porous matrix aggregate composed of sub-μm monomers. In addition, impact simulations

100 have typically been performed studying large-scale collisions or crater-forming events. Bland et
101 al. (2014) and Davison et al. (2016) performed numerical modeling of impacts at sufficient
102 resolution to inform the interpretation of features at 100's μm to cm-scale, i.e., providing an
103 impact simulation baseline appropriate for thin section petrographic studies, or analysis of small
104 meteorite aliquots, and in simulated materials that more closely approximate chondrites. The
105 ability to visualize shock at this 'meso-scale', and observe the effect of a shock wave on low-
106 porosity chondrules set in a high-porosity uncompacted matrix (70-80% porosity), was revealing.
107 Even at relatively low impact velocities (1-2km/s), impact induced compaction can have a
108 significant effect, and there is significant heterogeneity in shock effects at scales of ~100 μm
109 (Bland et al., 2014; Davison et al., 2016). Most notably, the matrix behaves very differently than
110 chondrules. The meso-scale simulations revealed that matrix in an Allende compaction scenario
111 would experience much higher post-shock temperature increase (ΔT(final) = 300-400K) than
112 chondrules, which are barely heated (ΔT(final) <20K). Chondrules act as a heat sink – matrix
113 rapidly equilibrates to a bulk post-shock temperature ~200K lower than matrix T(peak). These
114 impacts would generate negligible shock metamorphic textures in chondrule olivine, consistent
115 with assignment of an S1 shock level for Allende.

116 There is evidence from previous studies (Funaki and Wasilewski, 1999, 2000; Gattacceca et al.,
117 2005; Sugiura et al., 1985; Watson, 1983) that in addition to inducing a crystallographic/rock
118 fabric in Allende matrix, impacts also imparted a magnetic fabric. To determine the magnetic
119 fabric, these previous studies measured the anisotropy of magnetic susceptibility (AMS) of
120 Allende matrix and found an oblate magnetic fabric, which is the expected fabric to result from
121 impact. AMS is a popular approach for determining the magnetic fabric due to the speed of
122 measurement (Jackson, 1991), however, susceptibility measures the magnetic response of all the
123 minerals in a sample, i.e., both remanence carriers (ferromagnets *sensu lato*) and non-
124 remanence carriers (paramagnets and diamagnets), and as such does not necessarily reflect the
125 anisotropy of the minerals carrying the natural remanent magnetization (NRM).

126 Given that the NRM carrier phase is frequently located in matrix, does the magnetic remanence
127 carrier display a magnetic fabric, and what is the effect of matrix heating on the NRM carriers?
128 And if heated, does the magnetic phase record a thermomagnetic remanence, and if so what is
129 the origin of magnetic field? To answer these questions, we report a new magnetic study of
130 Allende. In addition to a standard paleomagnetic study we also conduct a fabric study of the
131 magnetic remanence plus an ancient-field intensity study (paleointensity) using modern calibrated
132 and non-calibrated, non-heating methods.

133

134 **2. Methods**

135 **2.1 Paleomagnetic analysis**

136 A 60×3×3mm section of the Allende meteorite was chosen for analysis, and split into 16 ~2-3 mm
137 cubes (Table 1), retaining their relative orientation with respect to each other. To isolate the
138 primary magnetization of the NRM, which is likely to have been super-imposed by secondary
139 magnetizations, we applied the standard non-heating paleomagnetic technique of step-wise
140 alternating-field (AF) demagnetization up to a maximum alternating field of 120 mT. As the
141 samples were small, to improve signal-to-noise ratios, we measured their remanent
142 magnetization characteristics on a 2G SQUID magnetometer at the University of Oxford, fitted
143 with triaxial, static AF demagnetization coils.

144 To determine the magnetic fabric of the magnetic remanence carriers, we measured the
145 anisotropy of magnetic remanence (AMR). Unlike AMS measurements, AMR measurements
146 isolate the magnetic fabric of the magnetic remanence carriers, and, additionally, AMR is simpler
147 to interpret than AMS; AMS data leads to non-unique interpretations: the magnetic response of
148 small grains (magnetically single-domain (SD)) and larger multi-domain (MD) grains is opposite to
149 each other; in AMS measurements SD grains display ‘inverse’ magnetic anisotropy; in AMR

150 measurements all grain-sizes give the same response (Jackson, 1991). The samples were
151 imparted with anhysteretic remanent magnetizations (ARM) in nine individual orientations within
152 the samples, following the protocol of Jelinek (1978). For this we used a peak-alternating field of
153 200 mT, with a bias field of 100 μT. Before the measurement, the samples were tumbling-AF-
154 demagnetized using a maximum 100 mT field, followed by static three-axis AF demagnetization
155 up to 200 mT. To impart the ARMs we used a Detech D-2000 AF Demagnetizer. To improve the
156 signal-to-noise ratio for the AMR study, the sixteen samples were combined in orientated pairs, to
157 make eight samples.

158 To better constrain the homogeneity of the magnetization in samples, estimates of the recorded
159 paleointensity were made. Traditionally paleointensity measurements are made by replicating the
160 remanence acquisition mechanisms in the laboratory; this essentially means replicating
161 thermoremanence acquisition by heating samples to high temperatures. Generally, meteoritic
162 materials are susceptible to chemical alteration on heating, so non-heating methods are
163 employed, though for thermally stable samples these methods are generally less accurate (Yu,
164 2006). With the exception of the Preisach paleointensity protocol (Muxworthy and Heslop, 2011),
165 all non-heating methods are relative methods that rely on a calibration factor that is often
166 determined by examining material that is of terrestrial origin, e.g., 'REM family' methods (Acton et
167 al., 2007; Gattacceca and Rochette, 2004). In this paper we employ the Preisach paleointensity
168 protocol that relies on a first-order model to predict the response and behavior of small magnetic
169 particles in materials, and compare the results to those from the REM' method (Gattacceca and
170 Rochette, 2004). The REM' method is the latest development of the REM method; rather then
171 determine just the ratio of the NRM to a laboratory induced saturating isothermal remanence
172 (SIRM), the REM' method compares the ratio of the NRM and SIRM AF demagnetization spectra,
173 thereby determining a series of REM estimates, one for each AF demagnetization step. Generally
174 in the middle of the spectra there is usually a plateau of consistent REM estimates. The REM'
175 intensity is the average of the REM estimates in the plateau region.

Both the REM' and Preisach techniques assume that the primary NRM is a thermoremanence (TRM) in origin, and not, for example, a thermo-chemical remanent magnetization. For both techniques the NRMs' AF demagnetization data is combined with the AF demagnetization data for a laboratory induced SIRM. No further measurements are needed for the REM' protocol (Gattacceca and Rochette, 2004). For the Preisach method, it is necessary to also measure a series of hysteresis measurements termed first-order reversal curves (FORC) (Roberts et al., 2000). This was done using a Princeton Measurements (now Lakeshore) high-field vibrating sample magnetometer (VSM) at the University of Southampton. In contrast to the original Preisach protocol (Muxworthy and Heslop, 2011), where normalization is undertaken by a single SIRM measurement, in this paper we use SIRM AF demagnetization spectra to normalize (Di Chiara et al., 2017). We also measured the standard hysteresis parameters: (1) coercive force H_c, (2) the remanent coercive force H_{cr}, and (3) the reduced remanent saturation magnetization M_{rs}/M_s.

To assess the magnetic mineralogy of the remanence carriers, three samples were imparted with a saturation isothermal remanence (SIRM), and continuously thermally demagnetized using an Orion three-axis low-field VSM at Imperial College London.

2.2 Macroscale and mesoscale modeling

Simulations of the impact processing on the macro- and mesoscale were performed using the iSALE shock physics code (Amsden et al., 1980; Collins et al., 2004; Wünnemann et al., 2006). Porosity was modeled using the ε-α porous compaction model (Collins et al., 2011; Wünnemann et al., 2006). The ANEOS equation of state table for forsterite (Benz et al., 1989) was used to describe the bulk material in macroscale simulations and both the chondrules and matrix in mesoscale simulations. Lagrangian tracer particles were used to track the peak pressures and temperatures throughout both the macroscale and mesoscale simulations. The macroscale

simulations included self-gravity (using the algorithm described in Barnes and Hut (1986)), so the full crater formation and collapse process could be simulated. Mesoscale simulations followed the methodology described in Davison et al. (2016). Randomly placed non-porous chondrules were surrounded by porous matrix. Matrix abundance was set to 70%, and initial matrix porosity was 0.7 (leaving an initial bulk porosity of ~ 0.5). The initial temperature was set to 400 K. An impact velocity of 1 km/s was chosen to give a final matrix and bulk porosity consistent with Allende.

3 Results

3.1 Identification of primary magnetization directions.

In 14 of the 16 samples, a high-coercivity (HC) remanent magnetization component with unblocking fields > 20 mT was identified; in all samples, the NRM did not fully demagnetize by 120 mT, but the HC component was tending towards the origin (Fig. 1). Principal component analysis (PCA) was used to fit the components (Kirschvink, 1980). Plotting the directions on an equal area projection plot (Fig. 2), the HC components are clearly clustered (α_{95}=6.5˚), whilst the more poorly defined low-coercivity (LC) components are scattered. These results are in agreement with previous work for Allende matrix, which identified a HC unidirectional magnetization (e.g., Banerjee and Hargraves, 1972; Butler, 1972; Carporzen et al., 2011; Fu et al., 2014; Nagata, 1979; Sugiura et al., 1985; Sugiura and Strangway, 1985; Wasilewski, 1981)

3.2 Hysteresis parameters

The samples' displayed near consistent hysteresis parameters (Table 1). In terms of domain state these parameters are indicative of large pseudo-single-domain/MD material. The coercive force values (Table 1) are too high for MD magnetite, and are more indicative of iron sulphides.

Two FORC diagrams are show in Fig. 3. As a first-order approximation, the x-axis of a FORC diagram can be interpreted as the coercive force distribution, whereas spreading on y-axis is representative of magnetic interactions within the system, both inter-grain magnetostatic interactions and/or internal interactions within multidomain grains (Roberts et al., 2014). Fig. 3a is representative of all samples, except sample a1b (Fig. 3b). Fig 3a is typical of iron sulphides, which have relatively higher coercivity distributions than iron oxides and FeNi particles (Roberts et al., 2014). Sample a1b is distinctly different; it had a large chondrule near its surface that is very likely the cause of the anomalous magnetic behavior.

3.3 Thermomagnetic Analysis

The magnetization in two of the samples was mostly demagnetized (>95%) by 590–605K, suggesting the presence of pyrrhotite, which has a Curie temperature of ~595K (Dekkers, 1989), with a high-temperature tail persisting to >750K (Fig. 4). Pyrrhotite has been previously reported as the primary magnetic mineral in Allende matrix samples (Fu et al., 2014; e.g., Wasilewski, 1981; Weiss et al., 2010). Fu et al, (2014), determined a mean matrix composition of $Fe_{6.1}Ni_{2.8}S_{8.0}$, which for formation at <670K corresponds to an equilibrium assemblage of pentlandite, troilite and hexagonal pyrrhotite (Vaughan and Craig, 1978). The high-temperature tail is probably magnetite and awaruite as suggested previously (Funaki and Wasilewski, 2000), however, it has recently shown (Tarduno et al., 2016); that Allende matrix is highly unstable to heating, and acquires remanence even on heating in zero-field to < 620 K; for this to happen requires the creation of a new magnetic phase that is magnetically coupled to the existing remanence carrier. It is possible that the high-temperature tail observed in this study (Fig. 4) is an artifact created during this study.

248 The other sample (a1b), had not reached its Curie temperature by 1000K, indicating a Ni-poor
249 FeNi phase (Leedahl et al., 2016); this sample also had a NRM intensity six times greater than
250 the next strongest sample, and was one of the two samples for which HC and LC components
251 were not identified. As stated above sample a1b had a large chondrule near the surface.
252 Although not thought to be common, Ni-poor FeNi phases have been previously petrographically
253 identified in Allende chondrules (Emmerton et al., 2011).

254

255 **3.4 Anisotropy of ARM**

256 Only eight samples were used to determine the anisotropy, which is statistically low (Tauxe,
257 2010), however, the results from all eight samples were very consistent, especially with respect to
258 the minimum anisotropy axis (Fig. 5). The samples were found to be highly anisotropic (mean
259 P'=2.2 (Jelinek, 1981)), displaying a strong planar/oblate anisotropy (foliation, T=0.74, (Jelinek,
260 1981)), within which there is a preferred direction. The anisotropy reported here appears very
261 high compared to those reported in the literature for other minerals, but these should be
262 compared to the values for pure pyrrhotite samples, e.g., P'>40 (Louzada et al., 2010).

263 Previous magnetic fabric studies of Allende matrix all measured anisotropy of magnetic
264 susceptibility (AMS) (Funaki and Wasilewski, 1999, 2000; Gattacceca et al., 2005; Sugiura et al.,
265 1985); these studies all found an oblate anisotropy. Gattacceca et al. (2005) reported an
266 anisotropy value P ~ 1.09, which is much lower than the value reported here; however, AMR is
267 known to produce higher anisotropies than AMS, particularly for pyrrhotite-bearing samples
268 (Clement et al., 2008).

269

270 **3.5 Paleointensity determinations**

Both the REM' method (Gattacceca and Rochette, 2004) and the Preisach method (Di Chiara et al., 2017; Muxworthy and Heslop, 2011) were employed to determine paleointensity estimates (Table 1). For both paleointensity techniques, orthogonal projection plots (Fig. 1) are used to select the AF range of the component of interest, i.e., the HC component. The REM' paleointensity estimates are simply made by identifying an AF demagnetization range of the HC component for which the NRM/SIRM ratio is relatively constant, averaging this NRM/SIRM ratio and multiplying the average by 3000 to yield an estimate in micro-Tesla (Gattacceca and Rochette, 2004). The REM' method produced a narrow range of estimates (Table 1), with a mean of 12.2 ± 1.4 μT with a 95% confidence interval (CI_{95}) of 11–13 μT (Table 1).

The Preisach paleointensity method works by using the room-temperature-measured FORC diagram (Fig. 3) to generate a Preisach distribution (Muxworthy and Heslop, 2011; Muxworthy et al., 2011b). Using thermally activated Preisach theory, the measured Preisach distribution is used to predict the TRM/SIRM ratio as a function of applied field intensity. The predicted TRM/SIRM ratios are compared with the measured NRM/SIRM ratios to estimate the paleointensity. In a similar manner to the REM' procedure, to allow for multi-component magnetizations, the Preisach method determines paleofield estimates for each demagnetization step of the NRM (Fig. 1), and identifies areas of consistency (Di Chiara et al., 2017). The Preisach method allows for different cooling rates to be used in the paleointensity calculation. We considered three rates: 6 min, 1 hr and 24 hr to cool from the Curie temperature to ambient, though this range of cooling rates only contributed a difference of ~0.3 μT to the estimates. The mean estimate for the 1-hour cooling time was 5.9 ± 1.2 μT (CI_{95} 5 – 7 μT) (Table 1).

4. Discussion

Paleomagnetic analysis clearly demonstrated that the remanent magnetization within the Allende sample was uniform and the matrix's magnetic signal was dominated by pyrrhotite ($Fe_{(1-x)}S$ (x=0-

296 0.17)). In all but two of the samples, high-coercivity component directions were clearly aligned,
297 yielding a well-constrained mean direction with a 95% confidence cone (α_{95}) of 6.5˚ (Table 1).
298 Given the formation mechanism of the principal magnetic carrier phase (pyrrhotite) - a component
299 of the μm to sub-μm matrix material that is interstitial to the mm-sized spherical chondrules - the
300 uni-directional HC magnetic remanence must be post-accretional. This is in agreement with
301 previous studies, which have also found a consistent unidirectional magnetization in the Allende
302 matrix (e.g., Banerjee and Hargraves, 1972; Butler, 1972; Carporzen et al., 2011; Fu et al., 2014;
303 Nagata, 1979; Wasilewski, 1981; Weiss et al., 2010). Previous studies have also found on
304 thermal demagnetization of Allende NRM, this HC unidirectional magnetization aligns with the
305 'MT' (mid-temperature) component of the three component thermal demagnetization spectra
306 (Carporzen et al., 2011; Fu et al., 2014); the high-temperature (HT) component is only seen in
307 certain chondrules.

308

309 The paleointensity data also supports a coeval magnetization process throughout the sample.
310 The Preisach paleointensity estimates are lower than the REM' methods; from studies on
311 terrestrial historical lavas the Preisach method has been demonstrated to be more accurate than
312 the REM family of methods (Muxworthy et al., 2011b). We therefore take a paleofield estimate of
313 5.9 ± 1.2 μT, which has little inter-sample variation (Table 1) suggesting that they have recorded
314 the same field. Compared to other paleofield estimates for Allende bulk/matrix material, this value
315 is slightly lower than previous non-heating estimates: 12–18 μT (Wasilewski, 1981) and ~22 μT
316 (REM') by Emmerton et al. (2011), but lower than the 'AF estimate' of ~50–60 μT of Carporzen *et*
317 *al.* (2011), a Thellier (heating) estimate of > 100 μT (Banerjee and Hargraves, 1972) and a single
318 Preisach estimate of ~128 μT of Emmerton et al. (2011). The two differing Emmerton et al. (2011)
319 estimates are for the same sample; usually REM methods yield higher paleointensity estimates
320 than the Preisach method (Muxworthy et al., 2011b). The Emmerton et al. (2011) Preisach
321 palaeointensity estimate was determined using an earlier version of the method (Muxworthy et

al., 2011b); here we use the protocol outlined in Di Chiara et al. (2017). The Carporzen *et al.* (2011) study was not strictly non-heating as the estimates involved a thermal-calibration step. Generally, paleointensity estimates determined by heating protocols, e.g. Thellier-type approaches, yield higher estimates (Butler, 1972; Carporzen et al., 2011). Due to known irreversible alteration of the Allende matrix material above 50˚C (Tarduno et al., 2016; Wasilewski, 1981), these heating estimates should be treated with caution; Tarduno et al (2016) found that the Allende matrix acquires remanence even on heating in zero-field

Recent electron backscatter diffraction (EBSD) analysis (Bland et al., 2011; Watt et al., 2006) has found a pervasive uniaxial crystallographic fabric in Allende delineated by oriented matrix grains. Grain rotation occurred in response to impact shock, and an initially highly porous random aggregate of sub-μm fayalitic olivine grains was compacted to produce a uniaxial crystallographic matrix fabric (Bland et al., 2011; Watt et al., 2006). The AMR analysis of the magnetic fabric found the sample to be highly anisotropic (mean P' = 2.2 (Jelinek, 1981)), displaying a strong planar anisotropy (foliation, T=0.74, (Jelinek, 1981)), within which there is a preferred direction. The mean high-coercivity remanence direction of the NRM lies at 95% confidence ellipse within the easy-plane (Fig. 5). Given the high-anisotropy of the sample, it seems likely that the direction of the NRM is controlled/influenced to a degree by the intrinsic crystallographic fabric of the samples' matrix (Bland et al., 2011; Watt et al., 2006). This in turn supports a common, impact compaction mechanism for both the crystallographic and the magnetic fabric, which would have induced ordering of the matrix pyrrhotite grains' orientations, along with fayalitic olivine.

Given the planar nature of the fabric, we consider the most likely cause of the magnetic fabric to be an impact event. If impact generated, what information does this imply about the

346 magnetization process? What are the implications for the remanent magnetization? Is the
347 remanent magnetization controlled or affected by the impact? There are three scenarios:

348 1) the HC component of the NRM was formed at the same time as impact,
349 2) the HC component was formed pre-impact, and was rotated in to the plane,
350 3) the HC component was formed post-impact, and the magnetic-remanence direction was
351 strongly controlled by the existing fabric.

352 Impacts are thought to induce a remanent magnetization through one of two mechanisms: (1)
353 sufficient heating to induce thermomagnetic recording (Néel, 1955), and (2) piezomagnetism
354 (shock-magnetism) due to the interaction of the elastic and magnetic properties of a mineral
355 (magnetoelastic interaction) (Nagata, 1961); both mechanisms require the presence of an
356 external field. However, shock-magnetization is thought to only magnetize the low-coercivity
357 magnetic minerals (Cisowski and Fuller, 1978; Louzada et al., 2010), i.e., 'soft' magnetic minerals
358 that are unlikely to be stable over billions of years, whereas thermoremanent magnetizations
359 (TRM) have the potential to be stable over many billions of years (Néel, 1955).

360

361 Within the paleomagnetic community, it is generally considered that for a TRM to be induced,
362 high-shock pressures (>40 GPa) are required to produce sufficient heating (Weiss et al., 2010).
363 This level of shock (>S4 in ordinary chondrites) would generate pervasive shock metamorphism
364 throughout a meteorite. Allende is classified as stage S1 (shock pressures <5 GPa) -
365 macroscopic shock textures are absent (Scott et al., 1992). Peak-shock pressures <4-5 GPa are
366 thought to leave a meteorite unscathed, with no effects resulting from a post-shock temperature
367 increase of ~20K (Stöffler et al., 1991). In addition, although an impact may amplify an existing
368 field, and a transient field may be produced by an impact (Crawford and Schultz, 1988, 1993,
369 1999; Doell et al., 1970; Hide, 1972; Hood, 1987; Hood and Artemieva, 2008; Srnka, 1977), slow
370 cooling from a high post-shock temperature would not allow a magnetic phase to

371 thermomagnetically record the transient (minutes) field generated by a large impact (Weiss et al.,
372 2010). The assumption here is that even if an impact is large enough to produce a temperature
373 increase sufficient for a magnetic phase to record a TRM, because a large volume of the target is
374 affected, cooling will be slow. The consensus view therefore is that post-shock heating in CCs is
375 negligible – certainly too low to affect the paleomagnetic record in these rocks; and that while
376 impacts may well generate or amplify fields (Weiss et al., 2010), those fields are too brief to be
377 thermomagnetically recorded in the meteorite.

378

379 However, as discussed previously, this interpretation is founded on an empirical shock
380 metamorphism calibration (Stöffler et al., 1991), based on shock recovery experiments in non-
381 porous materials. Porous materials respond very differently, and as outlined in the introduction, it
382 is likely that primordial chondritic parent bodies had significant porosity. Pore-space compaction
383 attenuates shock energy and dramatically increases the amount of heating: a temperature
384 increase sufficient for a magnetic phase to record a thermomagnetic remanence is achievable,
385 even in a low-velocity collision. Impact modeling that accounts for the high porosity of primordial
386 matrix indicates that chondrite matrix could be heated to temperatures well above the Curie
387 temperature of pyrrhotite (~320°C) in even low-velocity collisions (1-2km/s), where bulk shock
388 pressure does not exceed 4GPa (Bland et al., 2014) – consistent with an S1 shock level. Thus,
389 TRM is possible in typical primitive parent body collisions. Indeed, in evolving from highly porous
390 primordial objects, to the meteorites that we see today, it is inevitable. If compacted by impact, all
391 chondrites would have been effected by this process. Therefore a pre-impact origin of the
392 remanence (scenario 2) can be excluded, because even low-velocity impacts are likely reset any
393 pre-existing magnetic remanence.

394

The assumption that slow cooling from a high post-shock temperature would not allow a magnetic phase to thermally record a transient field can also be deconstructed. It applies if the bulk post-shock temperature of the whole object exceeds the Curie point of the magnetic phase. With notable exceptions (e.g., Beitz et al., 2013), impact modeling and experiments assume uniform material properties in the target. In these scenarios, an estimate of bulk post-shock temperature has relevance in understanding heating at scales appropriate for interpreting meteorite data. But chondrites are not homogenous targets. More appropriately, they can be approximated as a target that has bimodal material properties – a fine-grained highly porous aggregate (matrix) juxtaposed against non-porous clasts (chondrules). In this scenario, bulk post-shock temperature does not provide a useful guide to interpreting meteorite data. Bland et al. (2014) and Davison et al. (2016) showed that impact-induced compaction results in significant matrix-heating, but that chondrules are largely unaffected. The result is a localized, transient temperature 'spike' in matrix, as chondrules act as a heat sink. Davison et al. (2016) performed a simple finite difference calculation to solve the heat conduction equation and estimate the timescale for temperature equilibration. They found that this timescale is dependent on the final matrix porosity, but for impact scenarios consistent with Allende, the matrix and chondrules likely equilibrated on the order of 10s seconds. This behavior has significance in understanding the paleomagnetic record in meteorites. Specifically, in a scenario where matrix is heated higher than the Curie point of the magnetic phase, but matrix and chondrules together equilibrate to a bulk post-shock temperature that is less than the Curie point, a matrix magnetic carrier phase would record a thermomagnetic remanence from any ambient field – stable or unstable, transient or long-lived. We have used mesoscale impact modeling to explore scenarios consistent with observations from Allende (constrained by estimated initial porosity, current bulk and matrix porosity, and the strength of the impact-induced matrix fabric). In our mesoscale modeling we find that a 1km/s planar impact scenario provides a good match to Allende porosity and fabric data. A number of studies converge on a peak metamorphic temperature for Allende of ~600K (Bonal et al., 2007; Rietmeijer and Mackinnon, 1985; Weinbruch et al., 1994; Zanda et al., 1995). Even assuming that

422 the impact occurred long after peak metamorphism (in this scenario we consider a starting
423 temperature of 400K), we still find that a large fraction of matrix is heated above the pyrrhotite
424 Curie point, before being cooled rapidly below it (Figure 6). This ability of chondrites to essentially
425 record a 'snapshot' of any ambient field during impact-induced compaction significantly increases
426 the number of options for the origin of the field. Specifically, it opens up the possibility that we are
427 observing paleomagnetic evidence of transient or unstable fields.

428

429 Therefore, if the remanent magnetization was acquired at the time of impact, for the
430 magnetization to still exist, the magnetization must be a thermoremanence. Basing their
431 hypothesis on Muxworthy et al. (2011a) (a precursor to Bland et al. (2014)), Fu et al. (2014) also
432 postulated this mechanism as the origin of the MT (=HC) component observed in the matrix and
433 the chondrules. As some of the chondrules also exhibit a HT component, the MT remanence
434 would, for these chondrules, be a partial rather than a full TRM. Fu et al. (2014) also considered
435 scenario (3), i.e., the remanent magnetization is post-impact; in this case the magnetization would
436 most likely be chemical/crystallization remanent magnetization (CRM). This CRM would have
437 been recorded during the formation of new pyrrhotite (aqueous metamorphism) in the presence of
438 a magnetic field of unknown origin, but this is reliant on the magnetic fabric of the newly formed
439 pyrrhotite grains being controlled by the existing crystallographic fabric, which is possible, though
440 the texture is not always fully inherited (Barrie et al., 2010; Craig and Vokes, 1993). Kojima and
441 Tomeoka (1996) and Krot et al. (1998) identified crosscutting iron oxides and sulfide phases,
442 suggesting post-impact formation; it likely that these phases formed in zero-field as the magnetite
443 signal does not appear to carry a remanence (Carporzen et al., 2011; Watson, 1983). These
444 crosscutting iron oxides and sulfide phases also appear isotropic and will likely not contribute
445 significantly to the magnetic fabric. Finally, in addition to the magnetic fabric it should be noted
446 that the relationship of iron oxide and sulphide veins (Kojima and Tomeoka, 1996; Krot et al.,
447 1998) to the larger Allende fabric measured later (via high-resolution EBSD analysis of matrix

448 (Bland et al., 2011; Watt et al., 2006) and CT analysis of larger components (Tait et al., 2016) has
449 not been established. Allende matrix remains highly porous ~40% (Bland et al., 2011). Whether
450 compaction was sufficient for veins to visibly rotate within that aggregate is unknown. In short,
451 more work is required to unambiguously determine the formation time and fabric (magnetic,
452 crystallographic and shape).

453

454 What is the origin of the recorded magnetic field? Studies have suggested that core-dynamos
455 within the CV and CM parent bodies are an explanation for the paleomagnetic record in
456 meteorites (Carporzen et al., 2011; Fu et al., 2014; Weiss et al., 2010). We have presented
457 evidence that potentially connects the paleomagnetic record in Allende to an impact that
458 compacted Allende matrix and generated a pervasive matrix fabric. This does not specifically
459 rule-out a core dynamo, but it does open up a variety of new possibilities to explain the
460 magnetization. External magnetic fields become a possibility. For external fields to be a viable
461 alternative to a core-dynamo requires that Allende must have been proximal to those fields.
462 Based on our estimated bulk P(shock) for Allende we can place some constraint on the position
463 of Allende within the parent body with respect to a wide range of impact scenarios. To do this we
464 employ the iSALE shock physics code (Collins et al., 2004; Wünnemann et al., 2006) to model
465 the macroscale pair-wise collision of planetesimals (e.g., Davison et al., 2012; Davison et al.,
466 2010). Bulk pore-space compaction was modeled using the ε-α porous compaction model (Collins
467 et al., 2011; Wünnemann et al., 2006)}, with both impactor and target given an initial bulk porosity
468 of 50%. The simulations included self-gravity (using the algorithm described in Barnes and Hut
469 (1986), so the full crater formation and collapse process could be simulated (Figure 7).
470 Lagrangian tracer particles tracked the peak pressure of material throughout the simulation. Peak
471 pressures in the range 1.25 to 2 GPa (appropriate for Allende, and highlighted in green in Figure
472 7) are routinely encountered relatively close to the crater, in the breccia lens. The meteorite could
473 have been exposed to an external field that impact-induced compaction allowed it to record.

474

475 There are two possibilities for an external field: an impact generated field and a disk field. The
476 magnitude of an impact generated field can be estimated based on scaling relations derived from
477 experimental data (Crawford and Schultz, 2000; Crawford and Schultz, 1999). The events that we
478 are concerned with are relatively large impacts into ~100km diameter parent bodies, where large
479 (transient) fields (orders of magnitude greater than the 11±4μT field that we observe in Allende)
480 appear to be possible (the value of the magnetic field experienced will depend on the position of
481 the material relative to the impact). There will be significant uncertainties in empirical scaling
482 relations, and discharge mechanisms may exist, but this experimental work suggests that Allende
483 could have been proximal to an impact-generated field far in excess of that required to explain the
484 paleomagnetic data. The second possibility is disk fields. Although the palaeomagnetic record in
485 CMs is similar to CVs, the interpretation is different: Weiss et al. (2010), Carporzen (2011), and
486 Fu et al. (2014) assume a core-dynamo in the case of the CVs, while Cournede et al. (2015)
487 highlight the possibility that CM chondrite magnetization might have an external (nebula) origin.
488 We agree, and extend that logic to the CVs. Our knowledge of the field strength and topology of
489 disk fields is limited: Fu et al. (2014) report that the Semarkona meteorite records a nebular field
490 of 54 ± 21 μT (1 -3 Myr), and Stephens et al. (2014) observe that a T Tauri star has a complex
491 magnetic structure. Magnetohydrodynamic (MHD) simulations predict 1–100μT fields in the mid-
492 plane at asteroidal distances (Bai and Stone, 2013; Gammie, 1996; Turner and Sano, 2008).
493 However, as Cournede et al. (2015) note, the disk has the potential to inherit a net vertical field
494 from the cloud in which it forms, which may then be modified by MHD turbulence moderated by
495 low ionization. The latest MHD results indicate that this may generate relatively stable fields
496 rather than the time-dependent ones found earlier: fields of order □10μT (Crutcher, 2012) to
497 100μT (Wardle, 2007), The CM and CV parent bodies would have been exposed to these fields in
498 the first 4 Myrs after CAI formation; recent Mn-Cr dating of secondary Ca-Fe silicates in CVs
499 obtained ages of 3.2 Ma after CAI (MacPherson et al., 2017), apparently cogenetic with fayalite

(and magnetite) and formed during alteration on the CV3 parent body. While there is some evidence to suggest that the solar nebula field had decayed by ~3.8 Ma after CAI (Wang et al., 2017), there is no data suggesting that it was absent at earlier times. CVs could have been exposed to a disk field following hydrothermal alteration and formation of secondary minerals at 3.2 Ma after CAI, and recorded that field during transient heating of matrix following impact-induced compaction.

5. Conclusions

This study has shown that the Allende matrix has a strong planar magnetic fabric: there is an easy magnetic plane, which is likely to have formed during impact. The high-coercivity component of the NRM is aligned with this easy magnetic plane, suggesting that the remanent magnetization direction is strongly influenced by the fabric. This is in agreement with previous studies (Sugiura et al., 1985). The NRM is either a thermoremanence formed during the impact or a chemical/crystallization remanent magnetization formed subsequent to impact (though in the latter case this would require pyrrhotite growth to be controlled by the pre-existing fayalitic olivine fabric). Our modeling indicates that a low intensity (~1km/s) impact into a simulated target would generate bulk and matrix porosity that are a match to Allende, as well as an impact-induced crystallographic matrix fabric consistent with observations (Bland et al., 2011). Importantly, this scenario would generate matrix heating sufficient to likely reset any previous remanent magnetization in the matrix, and because matrix heating is brief, it allows the magnetic carrier phase to record a transient or unstable field. We note that chondrites - bimodal mixtures of a highly porous matrix aggregate, and nominally zero porosity chondrules – constitute an impact target material that is uniquely capable of recording these events. Impacts into homogeneously porous targets, or low-porosity targets (e.g. planetary crusts (terrestrial impact craters)) generate less fine-scale heterogeneity in heating – bulk T_{final} is a useful proxy to T_{final} at fine scale. They

525 cannot record transient fields. The paleointensity estimates could not identify the origin of the
526 magnetic field, i.e., impact generated, planetesimal dynamo, or nebula etc. But an impact-
527 generated field or nebula field recorded during transient heating of matrix would provide an
528 explanation for the mutually orientated nature of the primary magnetization, without having to
529 invoke a paleofield and magnetization mechanism that is inconsistent with Allende's well
530 constrained low-temperature history and undifferentiated nature.

531

532 **Acknowledgements**

533 ARM would like to thank the paleomagnetism groups at the Universities of Oxford and
534 Southampton, for use of their equipment. ARM, GSC and TMD acknowledge the support of UK
535 STFC (grant ST/J001260/1). PAB would like to thank the Australian Research Council for support
536 under their Australian Laureate Fellowship scheme.

537

538 **References**

539 Acton G., Yin Q. Z., Verosub K. L., Jovane L., Roth A., Jacobsen B., and Ebel D. S. (2007) Micromagnetic
540 coercivity distributions and interactions in chondrules with implications for paleointensities of the
541 early solar system. *Journal of Geophysical Research* **112**(B3), B03S90.

542 Ahrens T. J. and Cole D. M. (1974) Shock compression and adiabatic release of lunar fines from Apollo 17.
543 In *Lunar and Planetary Science Conference*, pp. 2333–2345.

544 Amelin Y., Connelly J., Zartman R. E., Chen J. H., Goepel C., and Neymark L. A. (2009) Modern U-Pb
545 chronometry of meteorites: Advancing to higher time resolution reveals new problems. *Geochimica*
546 *et Cosmochimica Acta* **73**(17), 5212-5223.

547 Amsden A. A., Ruppel H. M., and Hirt C. W. (1980) SALE: A simplified ALE computer program for fluid flows
548 at all speeds, pp. 101. Los Alamos National Laboratories, Los Alamos.

549 Bai X.-N. and Stone J. M. (2013) Wind-driven accretion in protoplanetary disks 1. Suppresion of the
550 magnetorotational instability and launching of the magnetocentrifual wind. *Astrophysical Journal*
551 **769**(1).

552 Banerjee S. K. and Hargraves R. B. (1972) Natural remanent magnetizations of carbonaceous chondrites
553 and the magnetic field in the early solar system. *Earth and Planetary Science Letters* **17**(1), 110-
554 119.

555 Barnes J. and Hut P. (1986) A Hierarchical O(N-Log-N) Force-Calculation Algorithm. *Nature* **324**(6096), 446-
556 449.

557 Barrie C. D., Boyle A. P., Cook N. J., and Prior D. J. (2010) Pyrite deformation textures in the massive
558 sulfide ore deposits of the Norwegian Caledonides. *Tectonophysics* **483**(3–4), 269-286.

559 Beitz E., Guttler C., Nakamura A. M., Tsuchiyama A., and Blum J. (2013) Experiments on the consolidation
560 of chondrites and the formation of dense rims around chondrules. *Icarus* **225**(1), 558-569.

561 Benz W., Cameron A. G. W., and Melosh H. J. (1989) The origin of the Moon and the single-impact
562 hypothesis III. *Icarus* **81**(1), 113-131.

563 Bland P. A., Collins G. S., Davison T. M., Abreu N. M., Ciesla F. J., Muxworthy A. R., and Moore J. (2014)
564 Pressure-temperature evolution of primordial solar system solids during impact-induced
565 compaction. *Nature Communications* **5**, 5451-5451.

566 Bland P. A., Howard L. E., Prior D. J., Wheeler J., Hough R. M., and Dyl K. A. (2011) Earliest rock fabric
567 formed in the Solar System preserved in a chondrule rim. *Nature Geoscience* **4**(4), 244-247.

568 Blum J. (2004) Grain growth and coagulation. In *Astrophysics of Dust* (eds. A. N. Witt, G. C. Clayton, and B.
569 T. Draine), pp. 369-391.

570 Blum J. and Schrapler R. (2004) Structure and mechanical properties of high-porosity macroscopic
571 agglomerates formed by random ballistic deposition. *Physical Review Letters* **93**(11).

572 Bonal L., Bourot-Denise M., Quirico E., Montagnac G., and Lewin E. (2007) Organic matter and
573 metamorphic history of CO chondrites. *Geochimica et Cosmochimica Acta* **71**(6), 1605-1623.

574 Butler R. F. (1972) Natural remanent magnetization and thermomagnetic properties of Allende meteorite.
575 *Earth Planetary Science Letters* **17**(1), 120-128.

576 Carporzen L., Weiss B. P., Elkins-Tanton L. T., Shuster D. L., Ebel D., and Gattacceca J. (2011) Magnetic
577 evidence for a partially differentiated carbonaceous chondrite parent body. *Proceedings of the*
578 *National Academy of Sciences* **108**(16), 6386-6389.

579 Cisowski S. M. and Fuller M. (1978) The effect of shock on the magnetism of terrestrial rocks. *Journal of*
580 *Geophysical Research: Solid Earth* **83**(B7), 3441-3458.

581 Clement B. M., Haggerty S., and Harris J. (2008) Magnetic inclusions in diamonds. *Earth and Planetary*
582 *Science Letters* **267**(1-2), 333-340.

583 Collins G. S., Melosh H. J., and Ivanov B. A. (2004) Modeling damage and deformation in impact
584 simulations. *Meteoritics and Planetary Science* **39**(2), 217-231.

585 Collins G. S., Melosh H. J., and Wünnemann K. (2011) Improvements to the epsilon-alpha porous
586 compaction model for simulating impacts into high-porosity solar system objects. *International*
587 *Journal of Impact Engineering* **38**(6), 434-439.

588 Cournede C., Gattacceca J., Gounelle M., Rochette P., Weiss B. P., and Zanda B. (2015) An early solar
589 system magnetic field recorded in CM chondrites. *Earth and Planetary Science Letters* **410**, 62-74.

590 Craig J. R. and Vokes F. R. (1993) The Metamorphism of Pyrite and Pyritic Ores: An Overview.
591 *Mineralogical Magazine* **57**(386), 3-18.

592 Crawford D. and Schultz P. (2000) Electrostatically charged impact ejecta and implications for lunar
593 paleomagnetism. In *Lunar and Planetary Science Conference*, pp. 1849.

594 Crawford D. A. and Schultz P. H. (1988) Laboratory observations of impact-generated magnetic-fields.
595 *Nature* **336**(6194), 50-52.

596 Crawford D. A. and Schultz P. H. (1993) The production and evolution of impact-generated magnetic-fields.
597 *International Journal of Impact Engineering* **14**(1-4), 205-216.

598 Crawford D. A. and Schultz P. H. (1999) Electromagnetic properties of impact-generated plasma, vapor and
599 debris. *International Journal of Impact Engineering* **23**(1), 169-180.

600 Crutcher R. M. (2012) Magnetic Fields in Molecular Clouds. *Annual Review of Astronomy and Astrophysics*
601 **50**(1), 29-63.

602 Davison T. M., Ciesla F. J., and Collins G. S. (2012) Post-impact thermal evolution of porous planetesimals.
603 *Geochimica et Cosmochimica Acta* **95**, 252-269.

604 Davison T. M., Collins G. S., and Bland P. A. (2016) Mesoscale modeling of impact compaction of primitive
605 solar system solids. *Astrophysical Journal* **821**(1), 68-68.

606 Davison T. M., Collins G. S., and Ciesla F. J. (2010) Numerical modelling of heating in porous planetesimal
607 collisions. *Icarus* **208**(1), 468-481.

608 Dekkers M. J. (1989) Magnetic properties of natural pyrrhotite II. High- and low-temperature behaviour of Jrs
609 and TRM as function of grain size. *Physics of the Earth and Planetary Interiors* **57**, 266-283.

610 Di Chiara A., Muxworthy A. R., Trindade R., and Bispo-Santos F. (2017) Paleoproterozoic geomagnetic field
611 strength from the Avanavero mafic sills, Amazonian Craton, Brazil. *Earth and Planetary Science*
612 *Letters*(in review).

613 Doell R. R., Gromme C. S., Thorpe A. N., and Senftle F. E. (1970) Magnetic studies of Lunar samples.
614 *Science* **167**(3918), 695-697.

615 Elkins-Tanton L. T., Weiss B. P., and Zuber M. T. (2011) Chondrites as samples of differentiated
616 planetesimals. *Earth and Planetary Science Letters* **305**(1-2), 1-10.

617 Emmerton S., Muxworthy A. R., Hezel D. C., and Bland P. A. (2011) Magnetic characteristics of CV
618 chondrules with paleointensity implications. *Journal of Geophysical Research* **116**, E12007.

619 Fu R. R., Lima E. A., and Weiss B. P. (2014) No nebular magnetization in the Allende CV carbonaceous
620 chondrite. *Earth and Planetary Science Letters* **404**(0), 54-66.

621 Funaki M. and Wasilewski P. J. (1999) A relation of magnetization and sulphidation in the parent body of
622 Allende (CV3) carbonaceous chondrite. *Meteoritics and Planetary Science* **34**, A39-A39.

623 Funaki M. and Wasilewski P. J. (2000) Pentlandite and magnetic anisotropy in Allende CV3 chondrite. In
624 *Lunar and Planetary Science Conference*, pp. 1148. Lunar and Planetary Institute, Houston.

625 Gammie C. F. (1996) Linear theory of magnetized, viscous, self-gravitating gas disks. *Astrophysical Journal*
626 **462**(2), 725-731.

Gattacceca J. and Rochette P. (2004) Toward a robust normalized magnetic paleointensity method applied to meteorites. *Earth And Planetary Science Letters* **227**(3-4), 377-393.

Gattacceca J., Rochette P., Denise M., Consolmagno G., and Folco L. (2005) An impact origin for the foliation of chondrites. *Earth and Planetary Science Letters* **234**(3-4), 351-368.

Hide R. (1972) Comments on the Moon's magnetism. *The Moon* **4**, 39.

Hood L. L. (1987) Magnetic-field and remanent magnetiszation effects of basin-forming impacts of basin-forming impacts on the moon. *Geophysical Research Letters* **14**(8), 844-847.

Hood L. L. and Artemieva N. A. (2008) Antipodal effects of lunar basin-forming impacts: Initial 3D simulations and comparisons with observations. *Icarus* **193**(2), 485-502.

Humayun M. and Weiss B. P. (2011) A common parent body for Eagle Station Pallasites and CV Chondrites. In *Lunar and Planetary Science Conference*, pp. Abstract #1507. Lunar and Planetary Institute, Houston.

Jackson M. (1991) Anisotropy of magnetic remanence - a brief review of mineralogical sources, physical origins, and geological applications, and comparison with susceptibility anisotropy. *Pure Applied Geophysics* **136**, 1-28.

Jelinek V. (1978) Statistical processing of anisotropy of magnetic susceptibility measures on groups of specimens. *Studia geophisica et geodetica* **22**, 50-62.

Jelinek V. (1981) Characterization of the magnetic fabric of rocks. *Tectonophysics* **79**, T63-T67.

Kieffer S. W. (1971) Shock metamorphism of Coconino Sandstone at Meteor Crater, Arizona. *Journal of Geophysical Research* **76**(23), 5449-&.

Kirschvink J. L. (1980) The least-squares line and plane and the analysis of paleomagnetic data. *Geophysical Journal of the Royal Astronomical Society* **62**, 699–718.

Kojima T. and Tomeoka K. (1996) Indicators of aqueous alteration and thermal metamorphism on the CV parent body: Microtextures of a dark inclusion from Allende. *Geochimica et Cosmochimica Acta* **60**(14), 2651-2666.

Krot A. N., Petaev M. I., Scott E. R. D., Choi B. G., Zolensky M. E., and Keil K. (1998) Progressive alteration in cv3 chondrites: more evidence for asteroidal alteration. *Meteoritics and Planetary Science* **33**, 1065-1085.

Leedahl B., Korolev A. V., Zhidkov I. S., Skornyakov S. L., Anisimov V. I., Belozerov A. S., Kukharenko A. I., Kurmaev E. Z., Grokhovskii V. I., Cholakh S. O., and Moewes A. (2016) Searching for pure iron in nature: The Chelyabinsk meteorite. *RSC Advances* **6**(89), 85844-85851.

Louzada K. L., Stewart S. T., Weiss B. P., Gattacceca J., and Bezaeva N. S. (2010) Shock and static pressure demagnetization of pyrrhotite and implications for the Martian crust. *Earth and Planetary Science Letters* **290**(1-2), 90-101.

Macke R. J., Consolmagno G. J., and Britt D. T. (2011) Density, porosity, and magnetic susceptibility of carbonaceous chondrites. *Meteoritics and Planetary Science* **46**(12), 1842-1862.

MacPherson G. J., Nagashima K., Krot A. N., Doyle P. M., and Ivanova M. A. (2017) 53Mn–53Cr chronology of Ca–Fe silicates in CV3 chondrites. *Geochimica et Cosmochimica Acta* **201**, 260-274.

665 Melosh H. J. (1989) *Impact Cratering: A Geologic Process*. Oxford University Press, New York.

666 Muxworthy A. R., Bland P. A., Collins G. S., Moore J. M., Davison T., and Ciesla F. J. (2011a)
667 Heterogeneous shock in porous chondrites: Implications for Allende magnetization. In *AGU Fall*,
668 pp. GP11B-07, San Francisco,.

669 Muxworthy A. R. and Heslop D. (2011) A Preisach method for estimating absolute paleofield intensity under
670 the constraint of using only isothermal measurements: 1. Theoretical framework. *Journal of*
671 *Geophysical Research* **116**, B04102.

672 Muxworthy A. R., Heslop D., Paterson G. A., and Michalk D. (2011b) A Preisach method for estimating
673 absolute paleofield intensity under the constraint of using only isothermal measurements: 2.
674 Experimental testing. *Journal of Geophysical Research* **116**, B04103, doi:10.1029/2010JB007844.

675 Nagata T. (1961) *Rock Magnetism*. Maruzen, Tokyo. pp. 350.

676 Nagata T. (1979) Metereorite magnetism and the early Solar-System magnetic-field. *Physics of the Earth*
677 *and Planetary Interiors* **20**(2-4), 324-341.

678 Néel L. (1955) Some theoretical aspects of rock magnetism. *Advances in Physics* **4**, 191–243.

679 Ormel C. W., Cuzzi J. N., and Tielens A. G. G. M. (2008) Co-accretion of chondrules and dust in the solar
680 nebula. *Astrophysical Journal* **679**(2), 1588-1610.

681 Rietmeijer F. J. M. and Mackinnon I. D. R. (1985) Poorly Graphitized Carbon as a New Cosmothermometer
682 for Primitive Extraterrestrial Materials. *Nature* **315**(6022), 733-736.

683 Roberts A. P., Heslop D., Zhao X., and Pike C. R. (2014) Understanding fine magnetic particle systems
684 through use of first-order reversal curve (FORC) diagrams. *Reviews of Geophysics*,
685 doi:10.1002/2014RG000462.

686 Roberts A. P., Pike C. R., and Verosub K. L. (2000) First-order reversal curve diagrams: a new tool for
687 characterizing the magnetic properties of natural samples. *Journal of Geophysical Research*
688 **105**(B12), 28461-28475.

689 Sahijpal S. and Gupta G. (2011) Did the carbonaceous chondrites evolve in the crustal regions of partially
690 differentiated asteroids? *Journal of Geophysical Research* **116**, E06004.

691 Sasso M. R., Macke R. J., Boesenberg J. S., Britt D. T., Rivers M. L., Ebel D. S., and Friedrich J. M. (2009)
692 Incompletely compacted equilibrated ordinary chondrites. *Meteoritics and Planetary Science*
693 **44**(11), 1743-1753.

694 Scott E. R. D., Keil K., and Stöffler D. (1992) Shock metamorphism of carbonaceous chondrites. *Geochimica*
695 *et Cosmochimica Acta* **56**(12), 4281-4293.

696 Sharp T. G. and de Carli P. S. (2006) Shock effects in meteorites. In *Meteorites and the Early Solar System*
697 *II* (eds. D. S. Lauretta and H. Y. McSween), pp. 653-677. University of Arizona Press, Tucson.

698 Srnka L. J. (1977) Critical velocity phenomena and LTP. *Physics of the Earth and Planetary Interiors* **14**(3),
699 321-329.

700 Stephens I. W., Looney L. W., Kwon W., Fernandez-Lopez M., Hughes A. M., Mundy L. G., Crutcher R. M.,
701 Li Z.-Y., and Rao R. (2014) Spatially resolved magnetic field structure in the disk of a T Tauri star.
702 *Nature* **514**(7524), 597-599.

703 Stöffler D., Keil K., and Scott E. R. D. (1991) Shock metamorphism of ordinary chondrites. *Geochimica et*
704 *Cosmochimica Acta* **55**(12), 3845-3867.

705 Sugiura N., Matsui T., and Strangway D. W. (1985) On the natural remanent magnetisation in Allende
706 Meteorite. *Lunar and Planetary Institute* **16**, 831-832.

707 Sugiura N. and Strangway D. W. (1985) NRM directions around a centimeter-sized dark inclusion in Allende.
708 *Journal of Geophysical Research* **90**(supplement), C729-C738.

709 Tait A. W., Fisher K. R., Srinivasan P., and Simon J. I. (2016) Evidence for impact induced pressure
710 gradients on the Allende CV3 parent body: Consequences for fluid and volatile transport. *Earth and*
711 *Planetary Science Letters* **454**, 213-224.

712 Tarduno J. A., O'Brien T. M., and Smirnov A. V. (2016) Does the magnetization of CV meteorites record a
713 parent body core dynamo? In *Lunar and Planetary Science Conference*, pp. Abstract #2609. Lunar
714 and Planetary Institute, Houston.

715 Tauxe L. (2010) *Essentials of Paleomagnetism*. University of California Press, Berkley.

716 Turner N. J. and Sano T. (2008) Dead zone accretion flows in protostellar disks. *Astrophysical Journal*
717 *Letters* **679**(2), L131-L134.

718 Vaughan D. J. and Craig J. R. (1978) *Mineral Chemistry of Metal Sulfides*. Cambridge University Press,
719 Cambridge, UK.

720 Wang H., Weiss B. P., Bai X.-N., Downey B. G., Wang J., Wang J., Suavet C., Fu R. R., and Zucolotto M. E.
721 (2017) Lifetime of the solar nebula constrained by meteorite paleomagnetism. *Science* **355**(6325),
722 623-627.

723 Wardle M. (2007) Magnetic fields in protoplanetary disks. *Astrophysics and Space Science* **311**(1-3), 35-45.

724 Wasilewski P. J. (1981) New magnetic results from Allende C3(V). *Physics of the Earth and Planetary*
725 *Interiors* **26**, 134–148.

726 Watson G. S. (1983) Large sample theory of the Langevin distribution. *Journal of Statistical Planning and*
727 *Inference* **8**(3), 245-256.

728 Watt L. E., Bland P. A., Prior D. J., and Russell S. S. (2006) Fabric analysis of Allende matrix using EBSD.
729 *Meteoritics & Planetary Science* **41**(7), 989-1001.

730 Weinbruch S., Armstrong J., and Palme H. (1994) Constraints on the Thermal History of the Allende Parent
731 Body as Derived from Olivine-Spinel Thermometry and Fe/Mg Interdiffusion in Olivine. *Geochimica*
732 *et Cosmochimica Acta* **58**(2), 1019-1030.

733 Weiss B. P., Gattacceca J., Stanley S., Rochette P., and Christensen U. R. (2010) Paleomagnetic Records
734 of Meteorites and Early Planetesimal Differentiation. *Space Science Reviews* **152**, 341-390.

735 Wünnemann K., Collins G. S., and Melosh H. J. (2006) A strain-based porosity model for use in hydrocode
736 simulations of impacts and implications for transient crater growth in porous targets. *ICARUS*
737 **180**(2), 514-527.

738 Yu Y. J. (2006) How accurately can NRM/SIRM determine the ancient planetary magnetic field intensity?
739 *Earth and Planetary Science Letters* **250**(1-2), 27-37.

740 Zanda B., Bourot-Denise M., and Hewins R. H. (1995) Condensate Sulfide and Its Metamorphic
741 Transformations in Primitive Chondrites. *Meteoritics* **30**(5), 605-605.

742 Zel'Dovich Y. B. and Raizer Y. P. (1967) *Physics of Shock Waves and High-temperature Hydrodynamic*
743 *Phenomena*. Dover Publications, Mineola. pp. 944.

744

745 **Tables**

746

747 **Table 1.** Hysteresis parameters and paleofield intensity estimates for the subsamples.

748

sample	mass (mg)	*hysteresis parameters*			paleofield intensity estimation			
		H_c (mT)	H_{cr} (mT)	M_{rs}/M_s	range[a] (mT)	steps[b]	REM' (μT)	Preisach[c] (μT)
a1a	83.3	18	79	0.12	30 – 100	8	13.7 ± 0.4	7.8 ± 0.6
a1b	69.0	13	41	0.16	…[d]	…[d]	…[d]	…[d]
a2a	88.7	20	78	0.16	35 – 100	7	11.5 ± 0.6	5.7 ± 1.4
a2b	77.7	22	80	0.14	20 – 70	7	11.1 ± 0.3	4.0 ± 0.3
a2c	73.5	21	82	0.14	35 – 100	7	11.0 ± 0.4	…[e]
a2d	130.2	21	85	0.14	35 – 100	7	11.1 ± 0.3	5.7 ± 0.1
a2e	129.3	18	83	0.10	30 – 100	8	12.8 ± 1.0	6.6 ± 0.9
a2f	112.2	20	82	0.14	35 – 100	7	13.6 ± 1.0	5.7 ± 0.6
a2g	113.6	19	84	0.13	…[d]	…[d]	…[d]	…[d]
a2h	208.8	18	80	0.13	25 – 100	9	13.1 ± 1.0	6.4 ± 0.7
a3aa	64.8	19	77	0.14	50 – 100	5	13.7 ± 1.1	…[f]
a3ab	82.5	18	79	0.12	25 – 100	9	12 ± 2	5.7 ± 0.6
a3ba	49.5	19	76	0.15	30 – 70	6	13.5 ± 1.5	…[f]
a3bb	64.0	20	82	0.13	35 – 70	5	12.7 ± 1.0	…[f]
a4a	75.0	19	81	0.14	50 – 120	6	13.7 ± 0.4	7.3 ± 0.1
a4b	60.6	21	81	0.15	35 – 100	7	8.9 ± 1.0	4.1 ± 0.2

749 [a] Range over which the REMc and Preisach estimates were made.

750 [b] Number of AF demagnetization steps used in the REMc and Preisach estimations.

751 [c] Preisach estimate made using a cooling time of 1 hour to cool from the Curie temperature to ambient temperature.

752 [d] No estimate as no clear HC component identified.

753 [e] Measured FORC diagram of poor quality.

754 [e] No estimate as no clear palaeointensity range identified.

755

756

Figure captions

Figure 1. Two example orthogonal projection plots of the NRM AF demagnetization data from samples: (a) a2h and (b) a4a. For both samples HC and LC components are highlighted. Components are identified as segments of the demagnetization data that display straight lines. As the peak AF is increased, the samples become demagnetized and their magnetization's tend towards the origin of the projection plots.

Figure 2. Equal area projection plot showing the direction of both the HC and LC components of the 14 samples for which these were identified using orthogonal projection plots (Fig. 1). A mean direction for the HC components is calculated: 1) D is the declination of the mean HC direction in sample coordinates, 2) I is the is the inclinatoin of the mean HC direction in sample coordinates, 3) α_{95} is the 95% confidence ellipse of the mean HC direction, and 4) N is the number of HC directions used to determine the mean. Solid symbols are in the bottom hemisphere, open in the upper hemisphere.

Figure 3. FORC diagrams for samples: a) a1a and b) a1b. Sample a1a displayed a FORC diagram representative of most of the samples, sample a1b was anomalous in character. The smoothing factor is 5, and the averaging time is 100 ms.

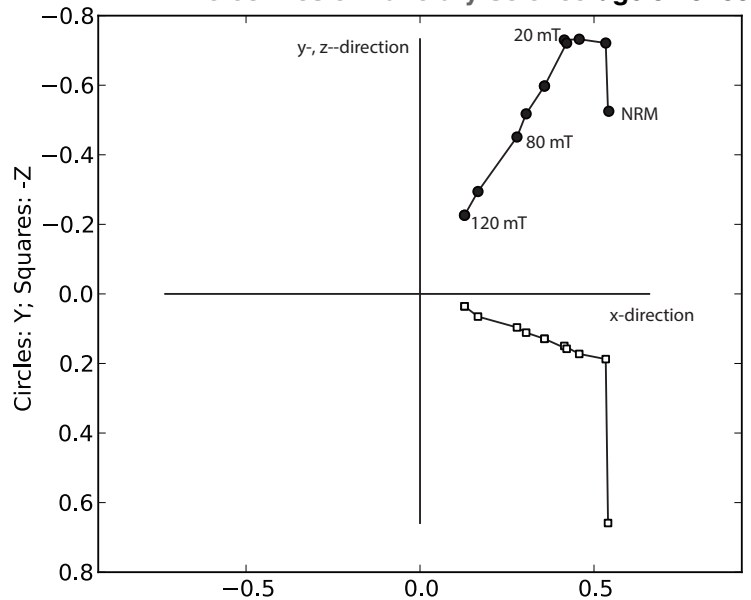
Figure 4. Continuous thermal demagnetization curve for sample a2h induced with a saturating isothermal remanent magnetization (SIRM) in a field of 1 T.

Figure 5. Lower hemisphere projections of the principal (squares), major (triangles) and minor (circles) eigenvectors with 95% confidence ellipses, determined by measuring the anisotropy of AARM. The confidence limits for the principal and major axes are quite large. For comparison the mean direction of the NRM HC component with 95% confidence ellipse is also plotted. D and I are the declination and inclination of the HC mean.

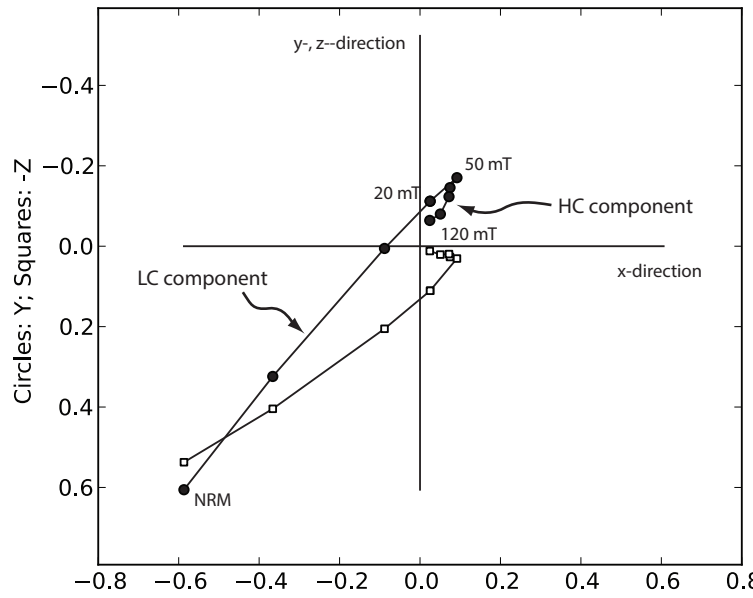
781 **Figure 6.** Mesoscale modeling, showing a 1km/s planar impact into a simulated carbonaceous
782 chondrite precursor with an initial 70:30 matrix:chondrule-volume ratio, an initial matrix porosity of
783 70%, and an initial temperature of 400K. The impact produces a material that has an Allende-like
784 matrix:chondrule mix, with bulk porosity (21%), matrix porosity (38%), and crystallographic fabric
785 intensity, that are a good match to the meteorite (Bland et al., 2011; Macke et al., 2011). A
786 number of studies converge on a peak metamorphic temperature for Allende of ~600K (Bonal et
787 al., 2007; Rietmeijer and Mackinnon, 1985; Weinbruch et al., 1994; Zanda et al., 1995). White
788 contours on the temperature plot separate the material that was heated above and that which
789 remained below the Curie temperature. Note that the matrix that remained cooler than the Curie
790 temperature was in the lee of the chondrules, where it was also less compacted by the shock
791 wave. The simulation shows that even at a conservatively low initial temperature of 400K, under
792 these conditions the majority of matrix is heated above the pyrrhotite Curie temperature.

793 **Figure 7.** Selections from macro-scale modeling of impacts between porous planetesimals for a
794 range of impactor and target body sizes. All have a constant initial temperature of 300K, bulk
795 porosity of 50% (the computational mesh does not resolve chondrule-scale heterogeneity at the
796 planetesimal scale so bulk porosity was parameterized), and impact velocity of 4km/s. The left
797 hand side of each model is at 250 sec after crater growth. Green tracer particles were shocked to
798 a pressure of 1.25-2GPa – fabric analysis and modeling indicate that the Allende protolith was
799 present in this region of the target.

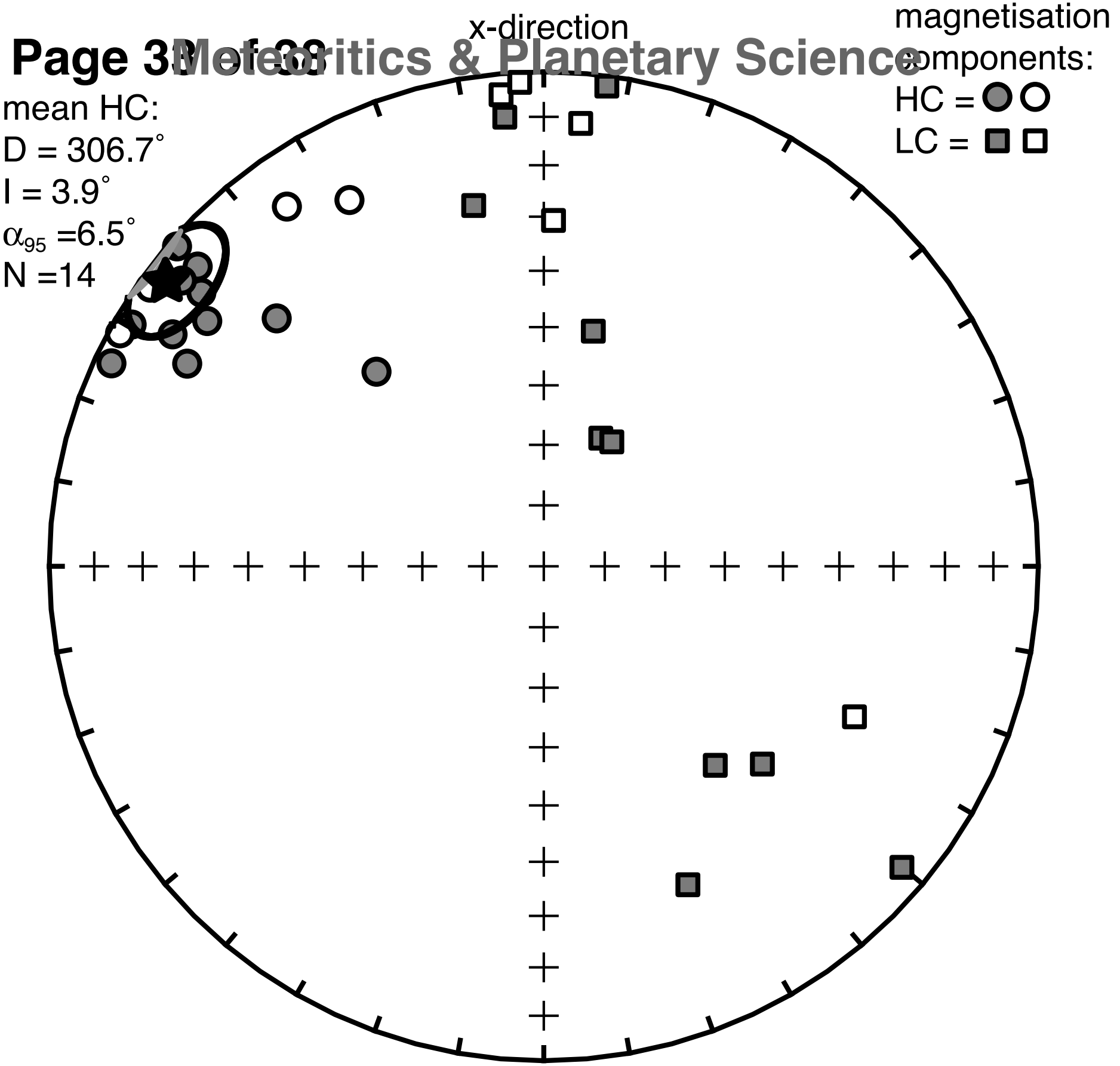
(a) sample a2h: specimen coordinates, normalized



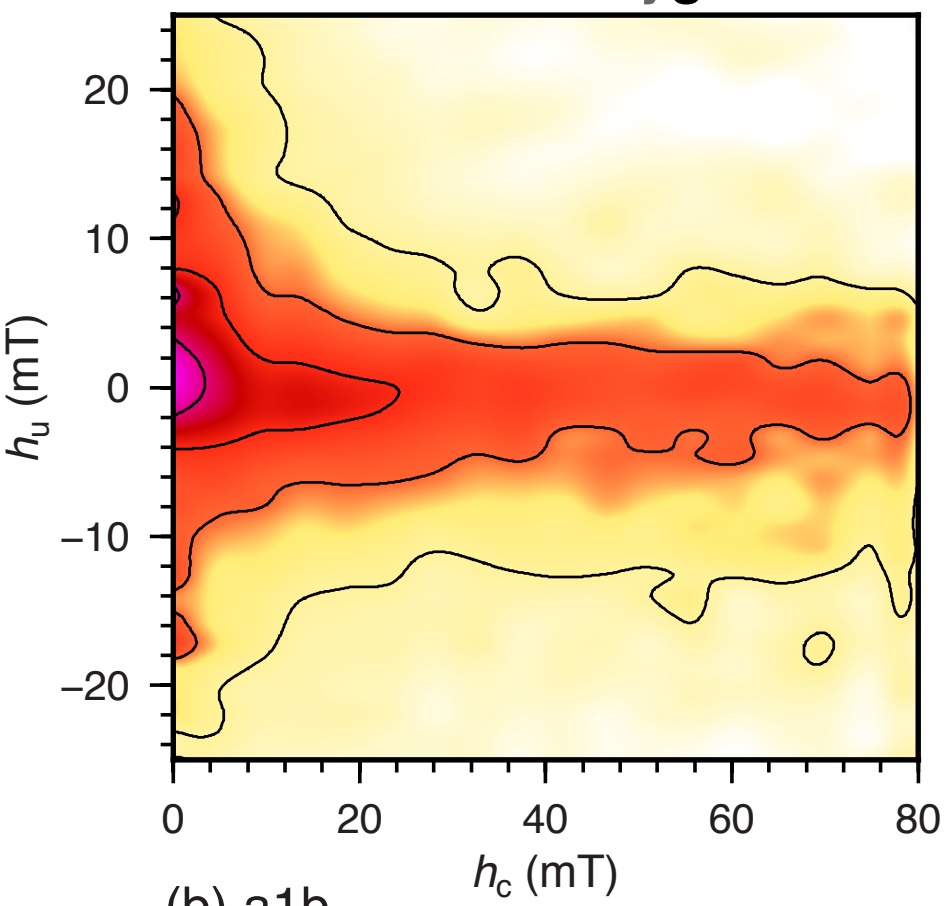
(b) sample a4a: specimen coordinates, normalized



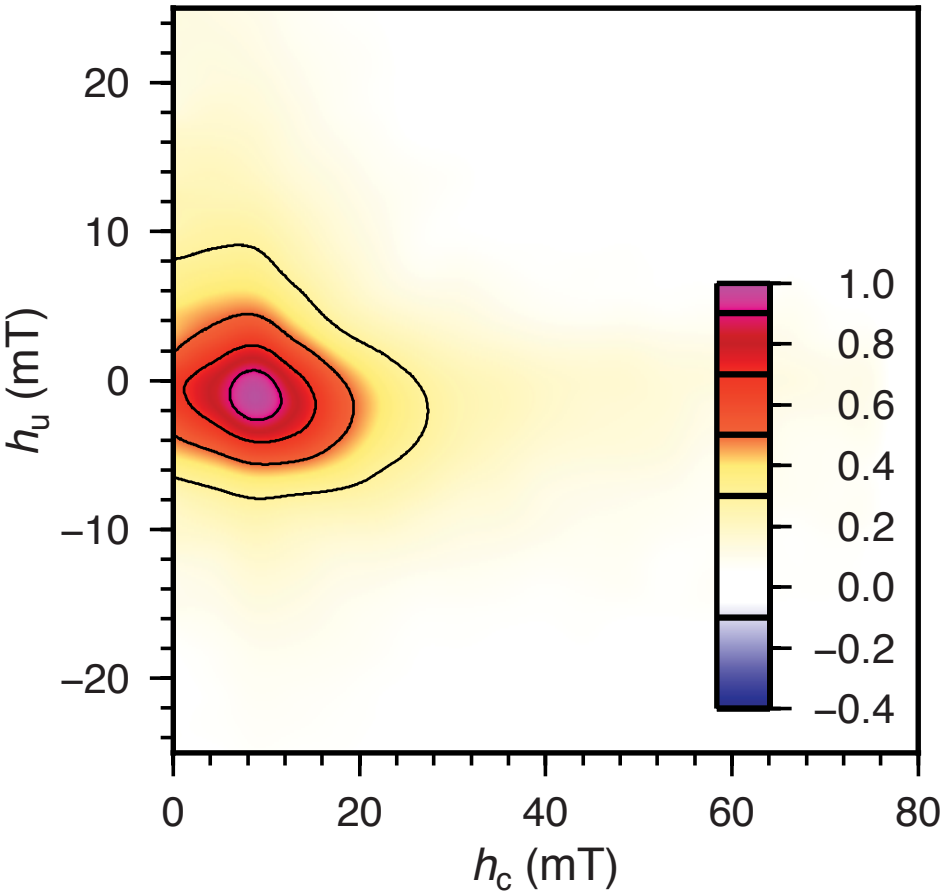
 Meteoritics & Planetary Science

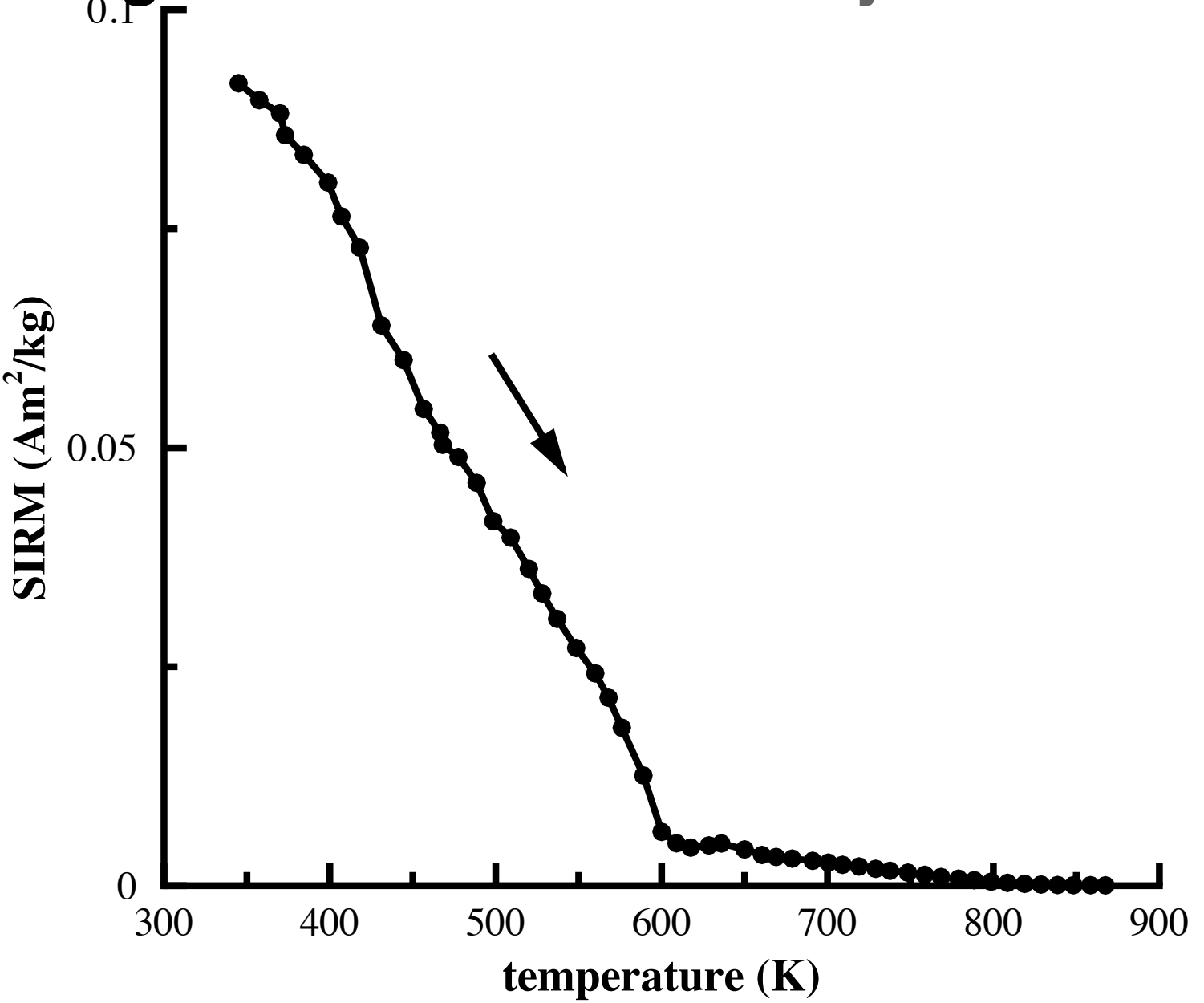


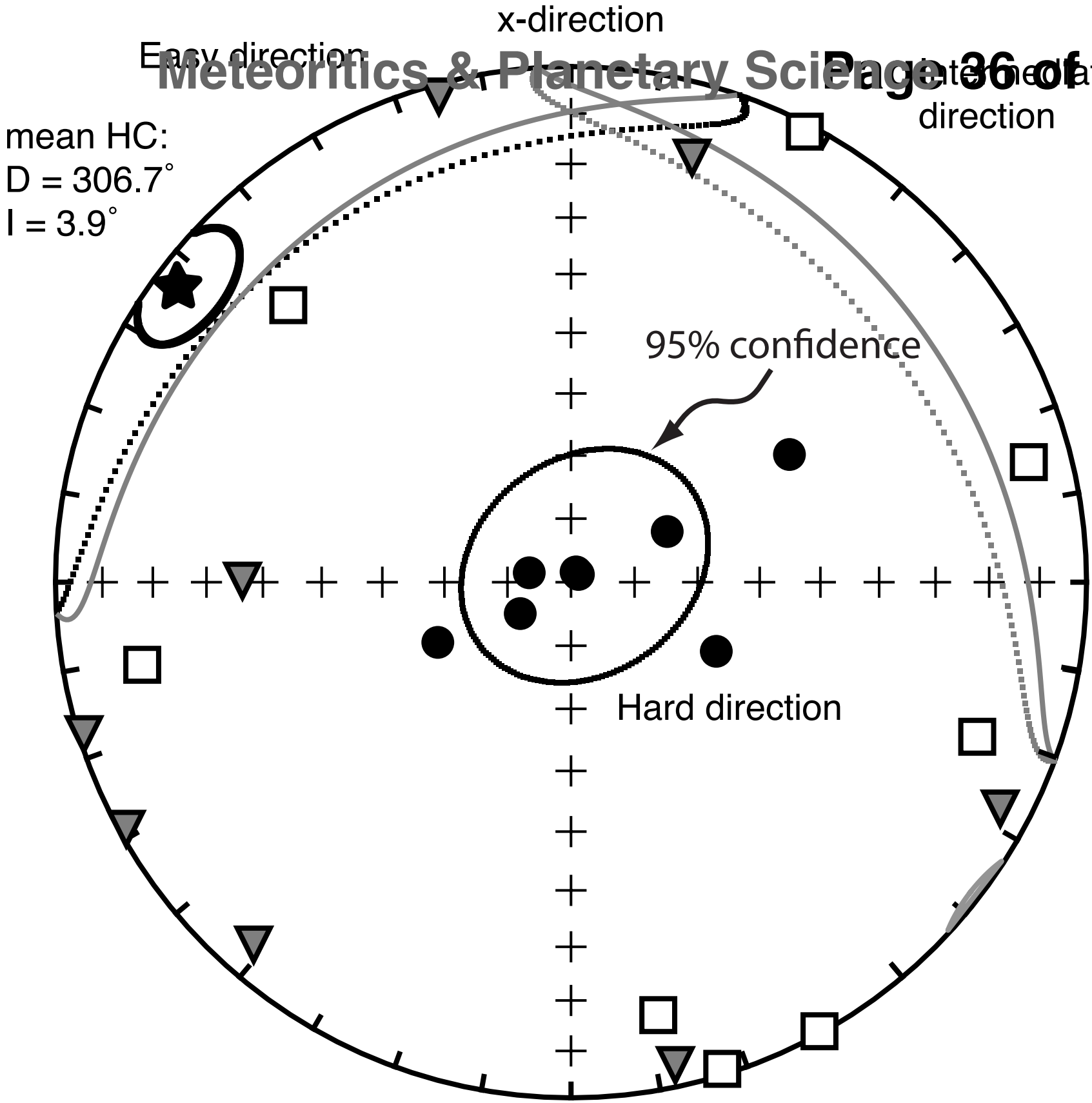
(a) a1a

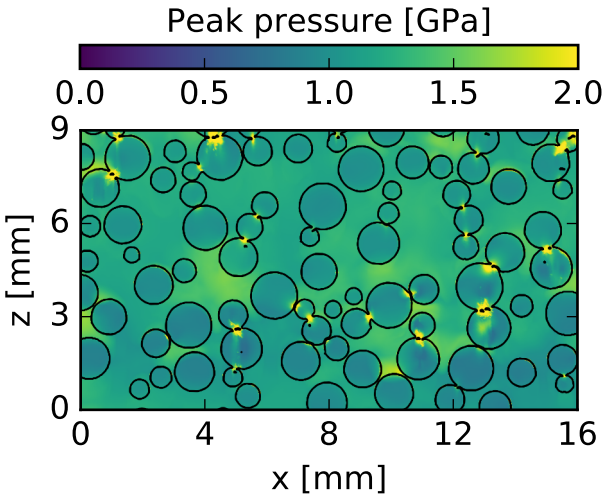

20
10
0
−10
−20
h_u (mT)
0
20
40
60
80
h_c (mT)

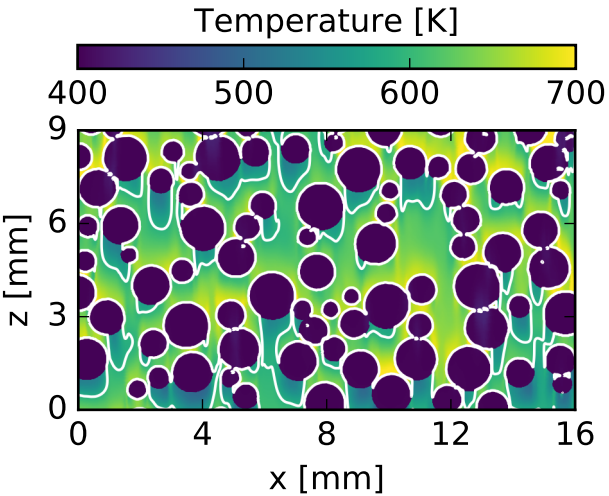
(b) a1b

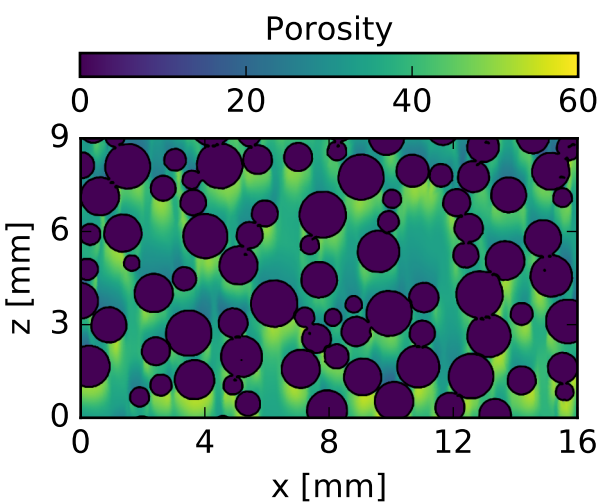

20
10
0
−10
−20
h_u (mT)
0
20
40
60
80
h_c (mT)
1.0
0.8
0.6
0.4
0.2
0.0
−0.2
−0.4

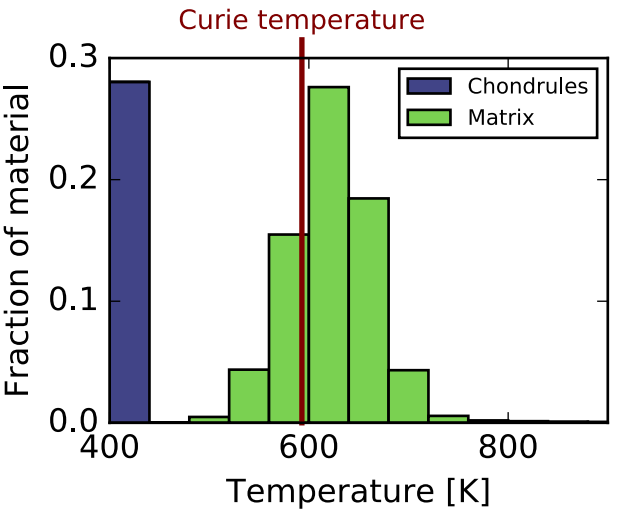

0.1
0.05
0
SIRM (Am²/kg)
300
400
500
600
700
800
900
temperature (K)

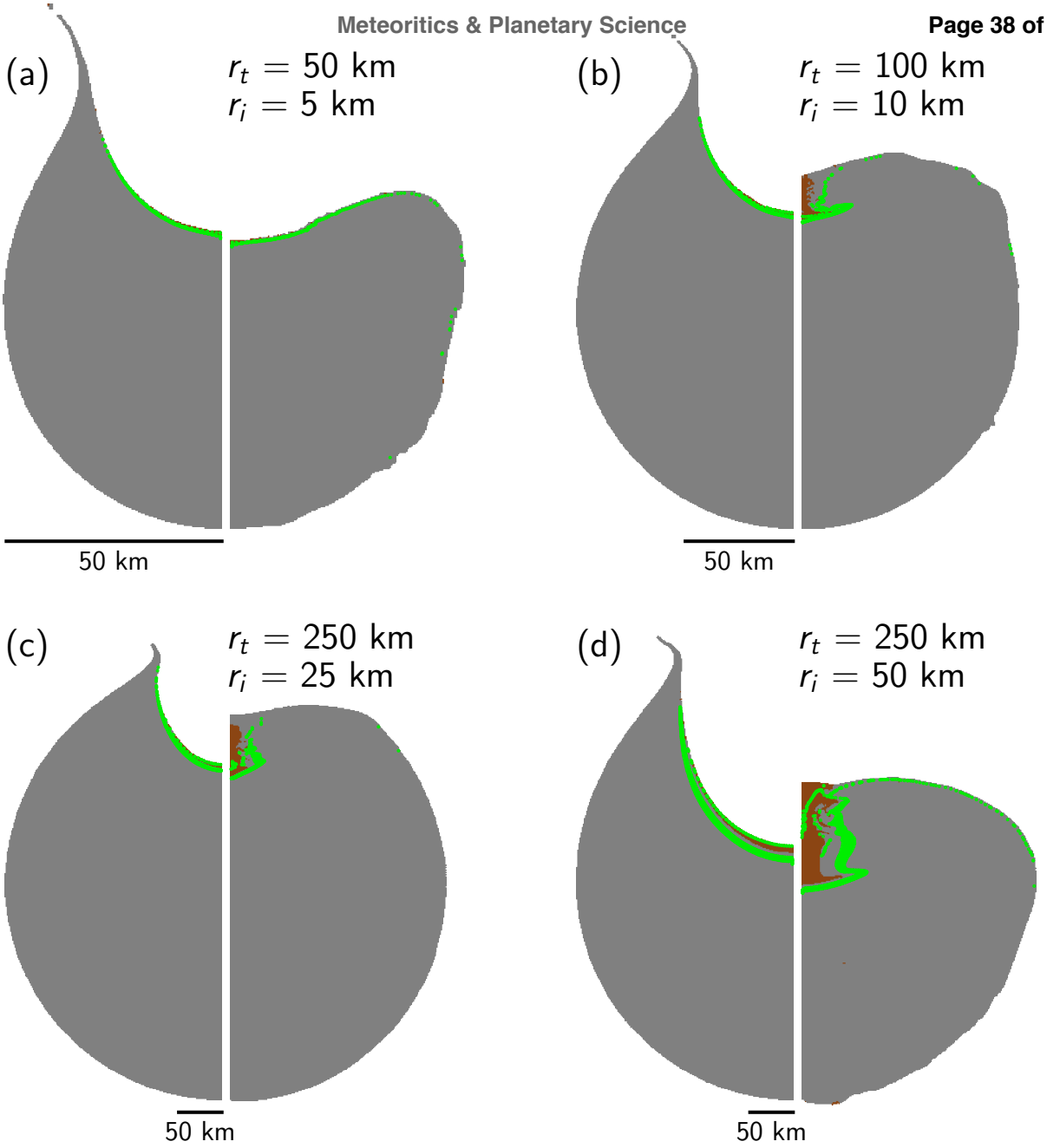

x-direction
Easy direction
Intermediate direction
mean HC:
D = 306.7°
I = 3.9°
95% confidence
Hard direction


Peak pressure [GPa]
0.0
0.5
1.0
1.5
2.0
z [mm]
x [mm]


Temperature [K]
400
500
600
700
z [mm]
x [mm]


Porosity
0
20
40
60
z [mm]
x [mm]


Curie temperature
Chondrules
Matrix
Fraction of material
Temperature [K]


(a)
r_t = 50 km
r_i = 5 km
50 km
(b)
r_t = 100 km
r_i = 10 km
50 km
(c)
r_t = 250 km
r_i = 25 km
50 km
(d)
r_t = 250 km
r_i = 50 km
50 km